Heat-Free Fabrication of Paper-Based Piezoresistive MEMS Devices via Mechanical Processing

Yahriel Salinas-Reyes,[1] Dr. Thomas Ward,[2] and Dr. Martin Thuo[3]

[1)]*Department of Aerospace Engineering, Iowa State University of Science and Technology.*

[2)]*Department of Mechanical and Aerospace Engineering, University of Virginia School of Engineering and Applied Science.*

[3)]*Department of Materials Science and Engineering, North Carolina State University*

(*Electronic mail: hgw8rs@virginia.edu.)

(Dated: 14 May 2024)

In an era characterized by rapid technological advancements, the integration of phase-change materials (PCMs) into piezoresistive Micro-Electro-Mechanical Systems (MEMS) sensors presents a promising avenue for enhancing their performance and functionality. This paper explores the theoretical underpinnings and practical applications of PCM-enhanced MEMS sensors, focusing on the optimization of sensor design and fabrication processes. The research methodology involves a comprehensive review of the literature on PCMs, MEMS sensors, and solid-to-solid phase transitions. Key findings reveal the potential of PCMs to revolutionize sensor technology by providing tunable mechanical properties, high sensitivity, and low power consumption. The implications of this study extend beyond the academic realm, with potential applications in biomedical applications, wearable electronics, selective modulation of electronic transport and environmental monitoring. By elucidating the fundamental principles governing PCM-based MEMS sensors, this research contributes to the broader understanding of phase-change phenomena and their role in next-generation sensor technologies.

This research investigates the integration of phase-change materials into piezoresistive MEMS sensors, aiming to enhance their performance and functionality through a comprehensive exploration of theoretical frameworks, experimental methodologies, and potential applications in various fields.

––––––––––––––––––––

I. INTRODUCTION:

The Piezoresistive (PZR) effect is an irreversible phenomenon observed in semiconductors with an impurity concentration, (i.e., doping atoms), during which mechanical force can be converted only into change in thermoelectrical resistance, not in electrical potential. Flexible-Tactile Sensors and micro-electro-mechanical-system (MEMS) built upon this principle can sustainably address microscale fabrication and instrumentation needs. A paper-based MEMS sensor is proposed where strain is proportional to mechanical stress with external power source.

High-efficiency (i.e. performance/cost ratio) in devices becomes harder to achieve as fabrication costs escalate and the assemblies of elegant high-performance devices require more sophisticated material-manufacturing systems. Conceptually, however, devices such as piezo transducers simply create connections between mechanical stimuli and electrical resistance changes, which can be achieved through simple, well-designed device architectures. This allows for development of low-cost instrumentation-measurement systems which can be tailored to capture any quantity of interest with which it is interfaced. Piezoresistive micro-electro-mechanical systems (MEMS) sensor devices are such examples of elegant, simple, efficient architectures which are highly-tunable for any function. We achieve these devices via an intuitive and frugal approach: prepared paper-base as substrate material which is green and abundant; bonded a carbon-graphite ink resistor pattern (strain gauge) to paper-base; applied thin-film electrodes via stencil process. Utilizing the fundamentals of kirigami/origami, piezoresistive theory, and heat-free soldering, such paper-based devices can prove to be a highly efficient and facile option for electronic devices while minimizing global impact on waste and energy. Furthermore, use of a soft meta-material (liquid-metal ink) and the deformability of papers leads to easier access to wider, more unique form factors and scalable designs, without increasing the cost of fabrication significantly, leading to simple assemblies of highly-tunable electronic devices that are mechanochemically-processed and disposable.

In this manuscript, guiding principals are introduced for probing the response of a power signal passed through a Piezoresistive Cantilevered Beam Sensor interfaced with a control volume. By transforming and processing signal from the transducer or sensing element, we visit the fundamental mathematical models for our paper-based scientific instrument and measurement system. The experimental method consists of a sensor calibration (To account for E-M coupling) and subsequent spectral analysis. While a power signal is passed through the sensor, the sensor tip position and deflection is also recorded. Next we further define our model and apply constraints to our problem. We can then derive beam properties and define a load in the controlled environment. After the signal has been anti-aliased, we start to build intuition about the response of our paper-based MEMS sensor by assuming ideal conditions in order to understand the dynamics taking place. Ultimately, this mathematical perspective serves as the foundation for elevating a frugally developed paper-based device to a highly-efficient measurement instrument.

II. MATERIALS AND METHODS

Using a multi-meter (D.C.), or alternatively, oscilloscope (A.C.) a voltage signal is supplied with a camera recording beam-tip position (Z). Image and signal processing were carried out to study electrical-mechanical behaviors that are encountered under ambient loads by varying form factors. The Piezoresistive Strain Gauge is bonded along a fixed-free cantilevered beam that is in-contact with a voltage-measurement system while subjected to mechanical stimuli (Beam-Body Deflection).

A. Device Fabrication

In fabricating a paper-based sensor, a precise, programmable paper cutter was used to make various sensor architectures (and shapes) and then bonded the piezoresistor and PCM contact pads to the paper substrate via a laser cut stencil. In further experiments in the development of a piezoresistive viscous shear sensor, a programmable laser cutter was used to create periodic nano-patterned cuts (kirigami) in the paper substrate. Subsequently the paper-base substrate was immersed in a bath of carbon resistive ink as the sensing element was adhered to the surface of the substrate. To introduce the mechanism of piezoresistive effects, a simple cantilever arm architecture. This is the process used to fabricate the device. We fabricated paper cantilever beams by cutting chromatography paper (0.34 mm thick) using a laser cutter. We manually screen-printed carbon resistors using high-resistivity graphite ink, and contact pads using low-resistivity sliver ink as a control. We generated a stencil mask by cutting designed patterns into vinyl stencil film using a laser cutter, placed the stencil mask on top of the patterned paper cantilever beams, filled the openings of the stencil mask with graphite ink, and removed the stencil mask to form the carbon resistor. We baked the paper device at 60 °C for 20 minutes. After the drying of the graphite ink, we screen-printed another layer of silver ink to form the contact pads following the same procedure. Fabricating an array of paper-based force sensors typically takes less than one hour. The subject of this paper and research, is to compare the fabrication processes, characteristics, and performance of the piezoresistive force sensors that use low-resistance silver paste as thin film electrodes to piezoresistive force sensors that are enhanced with Phase-Change Material thin film electrodes.

B. Electrical Characterization

Piezoresistor (PZR) Sensor Calibration Method. The Wheatstone Bridge is balanced using a single potentiometer where the PZR strain gauge is treated as the variable resistor. The power signal output is amplified using an instrumentation amplifier (INA) and the spectral content of the power or noise signal is measured using a signal analyzer function. The signal is analyzed alternatively by passing the signal through an antialiasing filter, sampled with an analog-to-digital converter

(ADC) and analyzed using the fast Fourier transform (FFT) method. The VBridge input into the wheatstone bridge was subject to DC (Direct Current) and AC (Alternating Current) bias throughout the measurements. The electro-mechanical coupling of the measurement system is accomplished through the PZR strain gauge bonded to the top surface of the table-top or cantilever beam.

C. Damping Mechanisms of Tip-Mass Piezoelectric System

By employing the Lumped model of bending electrostrictive transducers for energy harvesting, previous experimentation of damping mechanisms of a tip-mass piezoelectric system can be considered toward the piezoresistor force sensor system to develop a theoretical-numerical model for uniaxial loading (excitation). Theory of a tip-mass piezoelectric system can now be translated to a cantilevered piezoresistive system to study electromechanical and electrostrictive effects by applying similar boundary conditions and assumptions. This is done by defining the cantilevered piezoresistive sensor as an bending electrostrive transducer by considering only the forward piezoelectric effect, which is related to the piezoresistive effect, and disregarding the inverse piezoelectric effect. In other words, we only consider the feedback of the mechanical stimulation or excitation transduced into a power signal (which we observe/study as relative resistance change) and hold all other electromechanical quantities, energies, and degrees of freedom produced by the input power constant or reduced to zero. Here we characterize the damping response from a commercial piezoelectric transducer when it is subjected to free-vibrations. The problem under study is an electromechanical problem and hence a combination of dimensionless parameters including the natural frequency of the system, are used to study and understand the damping characteristics of the tip-mass-piezoelectric system. To directly visualize the tip displacement on the voltage generated, high-speed imaging studies of the cantilever are performed in addition to separate measurements of the voltage response using an oscilloscope.

D. Sensing Kirigami Principles

By employing programmable lasercutters and papercutters, we can adjust the mechanical properties of the paper substrate by applying principles of sensing kirigami. Paper is a modest material with rich affordances for craft and design. Paper comes in many different compositions. It can be shaped into delicate objects that move with the slightest touch; or constructed into robust structures that support a building. As designers and researchers, we are attracted to the qualities of paper for facilitating tangible interactions. We are particularly curious about kirigami a Japanese term we borrow to describe cutting, folding and bending flat sheets of paper into three-dimensional forms. Kirigami enables us to shape paper into pliable structures that move dynamically to afford tangible interactions. Our material-driven exploration is an-

chored in carbon-coated paper—an electrically resistive material affected by folding and bending. We investigated two types of paper for sensing tangible interactions and harnessed insights gained from them to inform three design propositions—tangible interfaces that range from part to product.

E. Theoretical Underpinnings:

To construct our ideal model, we make a number of assumptions and assume ideal conditions in all aspects of the experiment. The sensor therefore is a finite cantilevered beam with fixed-free boundary conditions and uniaxial loading (or excitation) on the top surface-place. Assuming an ideal thermo-mechanical system, the response to work-energy input on the MEMS is recorded as total deformation of the body ε and dimensionless power signal R^*. Therefore we define our principal axes in Fig [4] where longitudinal (beam-wise) strain ε_x is measured as well as lateral strain ε_y. The degree of deformation (i.e. Polarization) at a plane/spot is the total body deformation $\delta \propto \varepsilon$ and surface slope of θ. Equation [15] is a spot deflection approximation where the third term is the dynamic deflection coefficient of the surface $(\frac{Q}{\omega_n^3})^{1/2}$ and the Power Spectral Density (PSD) at the natural frequency for the ladder calculated from $\phi(t)$.

Approximating Real-World Beam Deflection:

$$\theta_{max} = \pi * \frac{\delta_{max}}{L} \tag{1}$$

$$\delta_{max} = g * (\frac{1}{32\pi^3})^{1/2}(\frac{Q}{\omega_n^3})^{1/2}(PSD)^{1/2} \tag{2}$$

$$\delta(X) = 77 * (\frac{X}{L})(\frac{Q}{\omega_n^3})^{1/2}(PSD)^{1/2}; \delta_X = \theta_X * X \tag{3}$$

$$\varepsilon = \sqrt{\varepsilon_x^2 + \varepsilon_y^2 + \varepsilon_z^2} = \frac{\delta_{max}}{L} \tag{4}$$

With geometry and relevant material,thermal, etc. properties in-hand, we may derive any of the following properties for the MEMS Sensor using the equations below. There are several other ways to approximate real-world beam deflection or force/energy terms which we will discuss later. But for the sake of simplicity, spot deflection $\delta(X)$ will assumed to capture the instantaneous motion of a spot in [mm]. This is explained in the section below.

Piezoresistive Theory:

$\rho = resistivity,$
$l = length,$
$\omega = width,$
$v = poisson's,$
$\varepsilon = strain.$

$$R_x = R = \frac{\rho l}{\omega^2} \tag{5}$$

$$\frac{\Delta R}{R_0} = (1 + 2v)\varepsilon + \frac{\Delta\rho}{\rho_0} \tag{6}$$

Applied Mechanics:

CURVATURE MODEL

$$\varepsilon_{flex} = \frac{Y}{R} \tag{7}$$

DEFORMATION MODEL

$$\varepsilon_{long} = \frac{\Delta l}{l} \tag{8}$$

$$\varepsilon_{lat} = \frac{\Delta\omega}{\omega} \tag{9}$$

F. Conservative Equations of Cantilevered Beam

- Euler-Bernoulli and Electric Current Conservation

- E-M Coupling and Tip-Mass

- Conservation of Moments and Force

- Dimensionless Variables for Damping and Free-Vibrations

In our system we define our time-series input $X(t)$ and power-energy signal as $\phi(t)$ with output signal $Y(t)$ and voltage drop $R(t)$. The signal has a frequency (f) and bandwidth "B".

We assume Parseval's Theorem [CITE] and arrive at the following:

$$X(t) = S_x(f) = \pi(\frac{f}{B}) \equiv |X(\hat{f})|^2 \tag{10}$$

Then Fourier Tables:

$$2B * sinc(2\pi Bt) \Leftrightarrow \frac{\pi f}{2B} \tag{11}$$

For a power-energy signal X(t) with auto-correlation function:

$$R_x(\tau) = 2Bsinc(2\pi Bt) \tag{12}$$

we have a anti-aliased Fourier Transform of the power signal $\phi(t)$ where $\delta(t) \equiv \phi(t) \equiv X(t)$ and τ is a standardized time constant.

$$S_x(f) = R_x(\hat{f}) = \frac{f\pi}{2B} \tag{13}$$

Compute total power of $X(t)$:

$$P_X = \int_{-\infty}^{\infty} R_x(f)\,df = \int_{-B}^{B} R_x(f)\,df \qquad (14)$$

$$R_x(f) = X(t) = \frac{V_{out}/2}{V_{in}} = \frac{sin(x)}{sinc(x)} = \frac{Response}{Input} \qquad (15)$$

Amplitude Response of Ideal Low Pass Filter (LPF):

$$|H(f)| = Y(t) = sinc(x) = \frac{sin(x)}{X} \qquad (16)$$

Where

$$|H(f)|^2 = \frac{\pi f}{B}$$

> *Fundamental Input-Output relation for Signals and Linear Time In-variant (LTI) Systems*
>
> $$S_Y(f) = |H(f)|^2 S_X(f)$$

Power Response:

$$P_Y = \int_{-\infty}^{\infty} S_y(f)\,df = \int_{-\infty}^{\infty} |H(f)|^2 S_X(f)\,df \qquad (17)$$

Therefore Power Output of the system:

$$P_Y = \int_{-\infty}^{\infty} S_y(f)\,df = B \qquad (18)$$

III. RESULTS

Liu1 developed principals for cantilevered PZR force sensors with conductive materials patterned on a paper substrate. The proposed fabrication technique enables heat-free rapid prototyping of such mechanically processed2 paper-based devices, as well as the development of highly-efficient (i.e., performance/cost) printable devices with varying electromechanical properties. In the absence of voltage-induced vibrations (D.C. voltage), calibration tests with fixed tip displacements were conducted to compute electro-mechanical coupling (K) of the PZR strain gauge. Alternatively, identical calibrations with A.C. bias measured device capacitive reactance. Resistance is the value of the piezoresistive component or material itself (Carbon Ink), while the reactance of a MEMS (Combination of all components) is quantified by system capacitance. The electromechanical coupling was found to depend heavily on paper-beam properties supported by fundamentals of PZR theory2 Table I,

- Energy Storage Efficiency Approximation

$$\frac{E_{Released}}{E_{absorbed}} = \frac{\sigma_V * K * \varepsilon}{(\sigma_m * \sigma_m * V)/(2 * E)} \qquad (19)$$

IV. DISCUSSION

Interest in synthetic composite materials has garnered significant attention, largely due to their high specific properties, tunable functionalities, and potential to incorporate advanced responsive behaviors. Recent advances have largely focused on stimuli-responsive composites, which exhibit tunable properties when subjected to a specified trigger. Such materials have been applied as sensors, actuators, and platforms for multifunctional devices. Mechanically reconfigurable parts are especially critical in soft robotics and analogous functional devices, whereby adaptive components are essential for controlled locomotion, actuation, stiffness tuning, and as deployable components. In particular, initially soft materials that can dramatically increase in rigidity and be programmed into desired shapes can be utilized in fields ranging from soft and bio-inspired robotics to reconfigurable and wearable electronics. Several forms of activation have been applied in responsive composites, and common examples include temperature, electromagnetic radiation, as well as electric and magnetic fields (Thuo, 2017). Recent developments in smart responsive composites have utilized various stimuli, including heat, light, solvents, electricity, and magnetic fields, to induce a change in material properties. Here, we report a thermodynamically driven mechanically responsive composite, exploiting irreversible phase-transformation (relaxation) of metastable undercooled liquid metal core-shell particle fillers (Salinas-Reyes et al., 2022). Thermal and mechanical analysis reveals that as the composite is deformed, the particles transform from individual liquid droplets to a solid metal network, resulting in a 300 percent increase in Young's modulus (Thuo, 2017). In contrast to previous phase change materials, this dramatic change in stiffness occurs autonomously under deformation, is insensitive to environmental conditions, and does not require external energy sources such as heat, light, or electricity. We demonstrate the utility of this approach by transforming a flat, flexible biocomposite strip of cellulose paper into a highly efficient and disposable piezoresistor that is highly sensitive, also referred to as Quantum Tunnelling Composites (QTCs) (Salinas-Reyes et al., 2022). The integration of phase-change materials (PCMs) into piezoresistive Micro-Electro-Mechanical Systems (MEMS) sensors holds promise for significantly enhancing their performance and functionality (Salinas-Reyes et al., 2022). This paper delves into the theoretical foundations and practical applications of PCM-enhanced MEMS sensors, focusing particularly on optimizing sensor design and fabrication processes. For the duration of this study, the focus was on synthesizing biocomposites with cellulose-based paper with heat-free fabrication processes. Printing of Conformal Solid Metal Traces on Non-Adhering Biological Surfaces offers a pathway to heat-free metal processing (Thuo, 2017). Metals and organics possess two very dissimilar surface energies, hence, do not naturally adhere to each other. This incompatibility is exacerbated by surface roughness, yet advances in wearables and bioelectronics call for their integration. Mesoscale mechanical bonds, however, transcend the necessities of surface energy matching while taking advantage of surface tex-

TABLE I. List of parameters used to characterize the electro-mechanical sensor

Non-Dimensional Variables[a]	Measured Variables [b]	Calculated Variables
Mechanical Strain (ε)	Volume of Body (V)	Mechanical Stiffness (E)
Relative Resistance ($\Delta R/R$)	Resistor Dimensions	Predicted Resistance (R)
Gauge Factor (K)	Mechanical Power (σ_m)	Electrical Resistivity (ρ)
Poisson's Ratio (v)	Tip Displacement (Z)	Beam Deflection (δ)
Dilation (e)	Voltage	Electrical Power (σ_V)

[a] Note a.

[b] Note b.

ture (Thuo, 2017). By conducting a thorough investigation of PCMs, MEMS sensors, and solid-to-solid phase transitions, this research aims to shed light on the transformative potential of PCMs in sensor technology. The utilization of PCMs offers the prospect of tunable mechanical properties, heightened sensitivity, and reduced power consumption, thereby revolutionizing sensor applications across various domains such as healthcare, aerospace, and structural monitoring. Dr. Thuo's Stabilization of Undercooled Metals via Passivating Oxide Layers relies on the frustration of liquid-solid transition mainly by an increase in activation energy (Thuo, 2017). This study not only contributes to academic knowledge but also holds implications for real-world technological advancements. The successful integration of phase-change materials into MEMS sensors is a testament to the interdisciplinary nature of modern research, which draws upon principles from materials science, mechanical engineering, and electrical engineering. The development of PCM-enhanced MEMS sensors underscores the importance of collaborative efforts aimed at addressing complex technological challenges. As we continue to push the boundaries of scientific inquiry, it is imperative to foster a culture of innovation and knowledge sharing, thereby propelling society towards a future characterized by technological excellence and sustainable development.

V. CONCLUSION

Paper-based MEMS sensors offer a satisfactory compromise between cost, simplicity, and performance of printable-flexible electronics. Advances in meta-materials and associated mechanical sintering enables ambient application of solid metallic contacts3 enabling heat-free fabrication of paper-based MEMS devices Efficiency values of MEMS are important in selecting reliable instrumentation as this describes the extent to which the input mechanical energy is stored, or transduced, into electrical energy of strain induced interactions. Alteration of the beam length of the body displayed the maximum degree of sensor modulation via origami/kirigami principles. Evidence concluded that the discussed paper-based piezoresistive sensors are ohmic in nature. The reviewed equations are the bare minimum for direct measurements from the MEMS sensor. We may further develop this mathematical model by delving deeper into mechanics of materials, thermofluids, fluid mechanics, beam theory, and all other Euler energy equations which may be involved. By transforming

the response signal of the sensor, for an ideal interaction, into qualities/quantities we can study to better understand the dynamics at play during these interactions of phase-change materials and interfacial phenomenon.
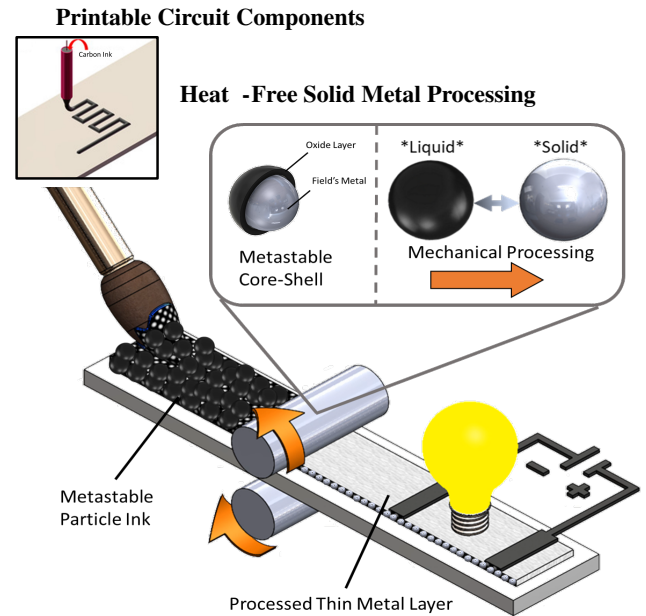
VI. FIGURES AND TABLES

Fig. 1

FIG. 1. A figure caption. The figure captions are automatically numbered.

Fig. 2

Fig. 3

Fig. 4

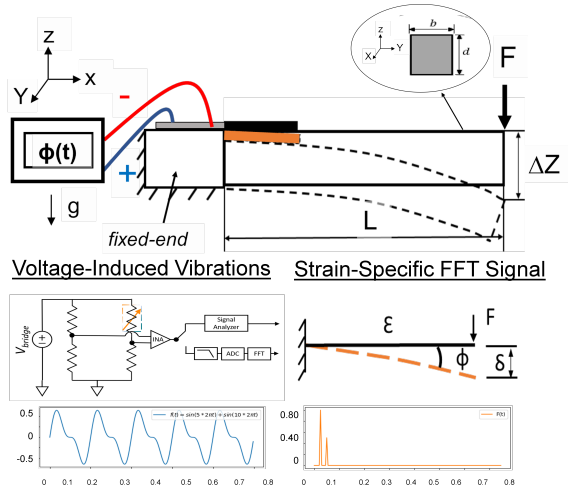Fig. 5

Fig. 6

Fig. 7

Fig. 8

Fig. 9

FIG. 2. Cantilevered Beam Model with beam cross-section and power signal, the power signal is produced as voltage-induced vibrations then is collected and analyzed by the measurement system and fast fourier transform (FFT) method.
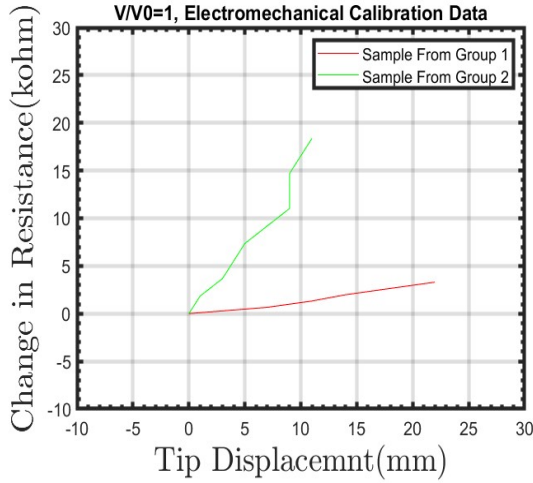

FIG. 3. A figure caption. The figure captions are automatically numbered.

FIG. 4. A figure caption. The figure captions are automatically numbered.

FIG. 5. A figure caption. The figure captions are automatically numbered.

Appendix A: Appendixes

Appendix B: MEMS Sensor Calibration and Beam Properties

Piezoresistor (PZR) Sensor Calibration Method. The Wheatstone Bridge is balanced using a single potentiometer where the PZR strain gauge is treated as the variable resistor. The power signal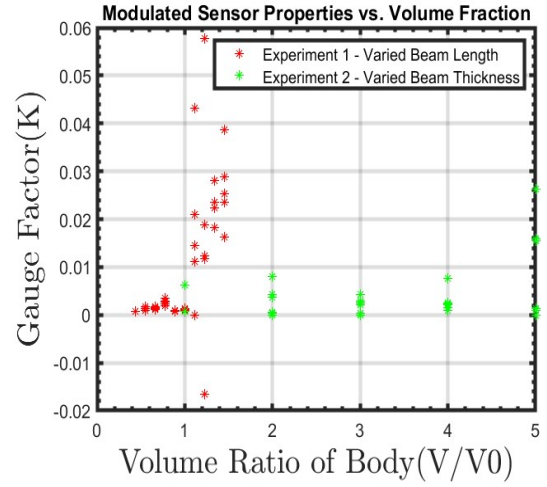 output is amplified using an instrumentation amplifier (INA) and the spectral content of the power or noise signal is measured using a signal analyzer function. The signal is analyzed alternatively by passing the signal through an antialiasing filter, sampled with an analog-to-digital converter (ADC) and analyzed using the fast Fourier transform (FFT) method. The VBridge input into the wheatstone bridge was subject to DC (Direct Current) and AC (Alternating Current) bias throughout the measurements. The electro-mechanical coupling of the measurement system is accomplished through the PZR strain gauge bonded to the top surface of the table-top or cantilever beam.

1. Equations and Theory

The corresponding mathematical equations for this process or operations are explained from the Direct Piezoresistive Ef-
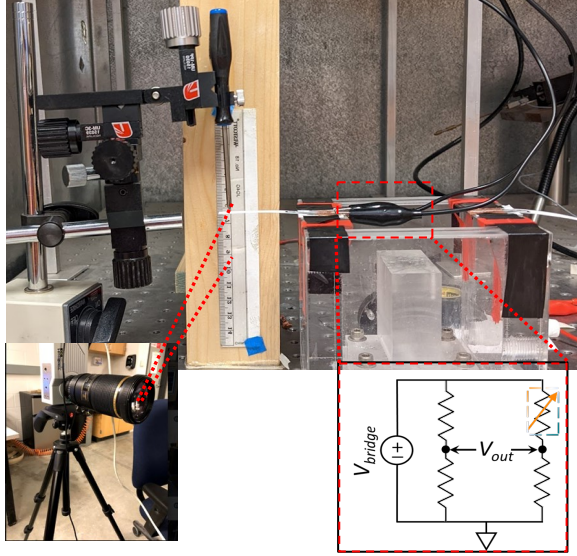
FIG. 6. Experimental Set-up with Monolithic Integration of a Signal Processing Circuit onto the Paper Device with high speed camera capturing beam tip position/deflection applied by micro-manager.
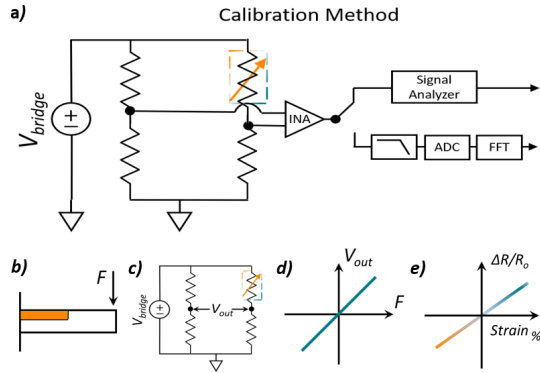
FIG. 7. (a) Example Calibration Measurement System. (b) Load applied to top surface of sensor with PZR Strain Gauge (orange) while tip position and deflection was recorded. (c) The PZR power signal ϕ is transduced using a RL circuit with with a wheatstone bridge configuration. (d) Calibration of the electro-mechanical coupling of PZR Sensor. (e) Derivation of dimensionless sensor properties (Gauge Factor = slope).

FIG. 8. Noise Measurement System and Signal Conditioning. The experimental set-up from the calibration method is modified with a AC biased Vbridge, a bandpass filter, and a low-pass filter in series with the sensor interface. The sensor at the interface is sensitive to electrical and any observable excitation in the environment (i.e. mechanical).

> *Piezoresistor Properties*
>
> δ = Beam-Body Deflection
> R = Strain Gauge or Resistor Signal
> ε = Strain
> ρ = Electrical Resistivity
> L = Resistor Length
> w = Resistor Width
> A = Resistor Conducting Area
> $\Delta R/R_0$ = Relative Change in Resistance
> K = Strain Gauge Factor/Electromechanical Coupling
> v = Poission's Ratio

$$\varepsilon = \frac{\delta}{L} \tag{B1}$$

$$R = \frac{\rho L}{w^2} = \rho \frac{L}{A} \tag{B2}$$

$$R = \frac{\Delta R}{R_0} = (1+2v)\varepsilon + \frac{\Delta \rho}{\rho_0}; R = K * \varepsilon \tag{B3}$$

$$K = \frac{\Delta R/R_o}{\varepsilon} = 1 + 2v + \frac{\Delta \rho/\rho_0}{\varepsilon} \tag{B4}$$

After the above equations have been correlated with the calibration data and spectral content, the strain gauge sensing element, or reciever, has now characterized the piezoresistive electro-mechanical coupling coefficient "K" of the sensing element (i.e., Gauge Factor). To summarize, this calibration method accounts for any variation or error from the piezoresistor or strain gauge itself across measurements.

With all or most of the material properties in hand along with strain readings, we can derive the mechanical behavior of the sensor as well as the stress-strain tensors by probing the

fect with the following properties. Hence we arrive at the following dimensional and dimensionless properties for the sensor in equations 1-4.

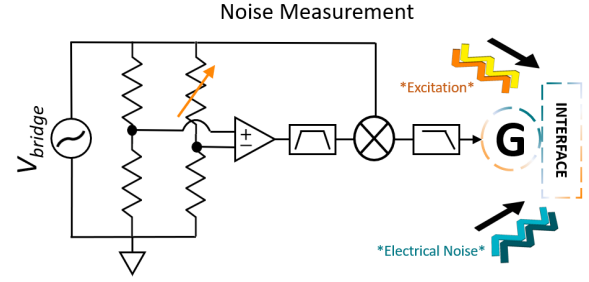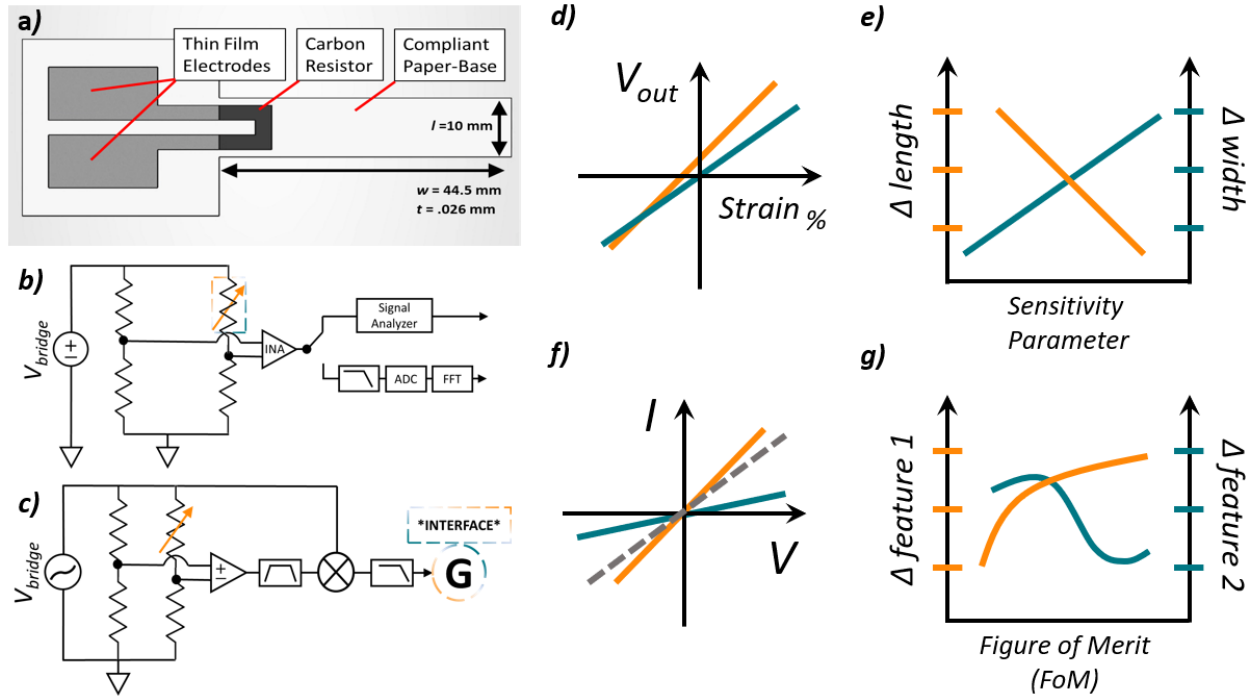FIG. 9. A figure caption. The figure captions are automatically numbered.

FIG. 10. Use the `figure*` environment to get a wide figure, spanning the page in `twocolumn` formatting.

deflection term δ (i.e. Strain). Hence we arrive at the stress-strain for normal stress and shear.

Stress-Strain Tensor

$$\varepsilon_x = \frac{\sigma_x}{E} - v\frac{\sigma_y}{E} - v\frac{\sigma_z}{E}$$

$$\varepsilon_y = -v\frac{\sigma_x}{E} + \frac{\sigma_y}{E} - v\frac{\sigma_z}{E}$$

$$\varepsilon_z = -v\frac{\sigma_x}{E} - v\frac{\sigma_y}{E} + \frac{\sigma_z}{E}$$

$$\gamma_{xy} = \frac{\tau_{xy}}{G}; \gamma_{yz} = \frac{\tau_{yz}}{G}; \gamma_{xz} = \frac{\tau_{xz}}{G}$$

Continuing on with our derivations, the mechanical or materials properties we are really concerned with are with are the gradient volume change across the sensor or dilation. Dilation is often caused by hydrostatic stress which is simply pressure that acts uniformly across a surface or material. This then defines the direction and hydrostatic load distrubuted throughout the material of the sample. Firstly, we need to transform the dilation vector "e" in terms of strain, to normal stress.

$$e = \varepsilon_x + \varepsilon_y + \varepsilon_z = \frac{1-2\nu}{E}(\sigma_x + \sigma_y + \sigma_z) \quad \text{(B5)}$$

Following this definition further, in the case of hydrostatic stress (p):

$$p = \sigma_x = \sigma_y = \sigma_z \quad \text{(B6)}$$

$$e = \frac{3(1-2\nu)}{E}p \quad \text{(B7)}$$

• Stoke's Theorem

Let Σ be a smooth oriented surface in R^3 with boundary $\partial\sum \equiv \Gamma$. If a vector field $F(x,y,z) = (F_x(x,y,z), F_y(x,y,z), F_z(x,y,z))$ is defined and has a continuous first order partial derivatives in a region containing Σ, then

$$\iint_{\Sigma} (\nabla \times F) \cdot d\Sigma = \oint_{\partial\Sigma} F \cdot d\Gamma \quad \text{(B8)}$$

• Euler-Lagrange Equation

$$\frac{d}{dt}\left(\frac{\partial L}{\partial \dot{q}_i}\right) - \frac{\partial L}{\partial q_i} = 0 \quad \text{(B9)}$$

The Euler-Lagrange equation is a fundamental equation in the field of analytical mechanics, specifically within the framework of Lagrangian mechanics. It provides a method to derive the equations of motion for a system based on a function called the Lagrangian, L, which represents the difference between the kinetic energy (T) and potential energy (V) of the system, $L = T - V$.

The equation emerges from the principle of stationary action, which states that the path taken by a system between two states, over a certain time, is the one for which the action integral (the integral of the Lagrangian over time) is stationary (usually a minimum). In mathematical terms, for a system described by generalized coordinates q_i and their time derivatives q_i', the Euler-Lagrange equation is expressed as given.

This equation determines how the coordinates q_i evolve over time, effectively describing the dynamics of the system under conservative forces. It is used widely across many fields of physics, including classical mechanics, quantum mechanics, and field theory, to derive the equations governing the motion of systems from molecular to astronomical scales.

TABLE II. **Population 1** Processing Conditions

Sample	Paper Beam			PZR					Sensor Properties				Measurements		
ID	l	ω	t	l	CSA	t	Loc	C.P.	GF	ν	ρ	$\Delta R/R_0$	ε_x	ΔR_x	$\Delta R/\Delta X$
1	64.15	10	0.26	8	46.25	0.0126	0	FM	2.83E-02	5.00E-01	1.10E+02	4.80E-03	1.70E-01	3.40E-04	4.00E-04
2	59.15	10	0.26	8	46.25	0.0126	0	FM	2.90E-02	5.00E-01	1.10E+02	5.38E-03	1.86E-01	3.71E-04	6.06E-04
3	54.15	10	0.26	8	46.25	0.0126	0	FM	3.27E-02	5.00E-01	1.10E+02	6.69E-03	2.05E-01	4.09E-04	1.25E-03
4	49.15	10	0.26	8	46.25	0.0126	0	FM	2.97E-02	5.00E-01	1.10E+02	6.79E-03	2.28E-01	4.57E-04	1.13E-03
5	44.15	10	0.26	8	46.25	0.0126	0	FM	3.08E-02	5.00E-01	1.10E+02	7.58E-03	2.46E-01	4.91E-04	1.80E-03
6	39.15	10	0.26	8	46.25	0.0126	0	FM	2.02E-02	5.00E-01	1.10E+02	7.99E-03	3.95E-01	7.89E-04	2.20E-03
7	34.15	10	0.26	8	46.25	0.0126	0	FM	6.72E-02	5.00E-01	1.10E+02	9.98E-03	1.48E-01	2.97E-04	2.30E-03
8	29.15	10	0.26	8	46.25	0.0126	0	FM	3.55E-02	5.00E-01	1.10E+02	1.40E-02	3.95E-01	7.89E-04	5.60E-03
9	24.15	10	0.26	8	46.25	0.0126	0	FM	3.69E-02	5.00E-01	1.10E+02	1.42E-02	3.84E-01	7.68E-04	6.50E-03
10	19.15	10	0.26	8	46.25	0.0126	0	FM	1.50E-02	5.00E-01	1.10E+02	1.21E-02	8.06E-01	1.61E-03	1.13E-02
11	37.63	10	0.26	8	46.25	0.0126	0	FM	3.71E-02	5.00E-01	1.10E+02	4.62E-03	1.25E-01	2.49E-04	3.00E-03
12	37.63	10	0.52	8	46.25	0.0126	0	FM	5.09E-02	5.00E-01	1.10E+02	8.82E-03	1.73E-01	3.47E-04	7.80E-03
13	37.63	10	0.78	8	46.25	0.0126	0	FM	1.47E-01	5.00E-01	1.10E+02	1.06E-02	7.19E-02	1.44E-04	2.26E-02
14	37.63	10	1.04	8	46.25	0.0126	0	FM	2.02E-01	5.00E-01	1.10E+02	1.66E-02	8.21E-02	1.64E-04	3.39E-02
15	37.63	10	1.3	8	46.25	0.0126	0	FM	2.58E-01	5.00E-01	1.10E+02	2.11E-02	8.21E-02	1.64E-04	4.36E-02
16	50	10	0.26	8	46.25	0.0126	0	FM	5.45E-02	5.00E-01	1.10E+02	1.22E-02	2.24E-01	4.48E-04	2.80E-02
17	50	10	0.26	12	66.25	0.0126	0	FM	3.62E-02	5.00E-01	1.58E+02	8.11E-03	2.24E-01	4.48E-04	3.84E-02
18	50	10	0.26	13	71.25	0.0126	0	FM	6.78E-02	5.00E-01	1.70E+02	1.52E-02	2.24E-01	4.48E-04	1.19E-02
19	50	10	0.26	14	76.25	0.0126	0	FM	5.04E-02	5.00E-01	1.82E+02	1.13E-02	2.24E-01	4.48E-04	2.29E-02
20	50	10	0.26	16	86.25	0.0126	0	FM	1.25E-01	5.00E-01	2.05E+02	2.80E-02	2.24E-01	4.48E-04	1.19E-01
21	50	10	0.26	8	46.25	0.0126	0	FM	8.09E-02	5.00E-01	1.10E+02	1.81E-02	2.24E-01	4.48E-04	2.74E-02
22	50	10	0.26	8	46.25	0.0126	5	FM	5.08E-02	5.00E-01	1.10E+02	1.14E-02	2.24E-01	4.48E-04	1.54E-02
23	50	10	0.26	8	46.25	0.0126	10	FM	5.62E-02	5.00E-01	1.10E+02	1.26E-02	2.24E-01	4.48E-04	1.49E-02
24	50	10	0.26	8	46.25	0.0126	15	FM	1.94E-01	5.00E-01	1.10E+02	4.34E-02	2.24E-01	4.48E-04	1.36E-01
25	50	10	0.26	8	46.25	0.0126	20	FM	5.31E-02	5.00E-01	1.10E+02	1.19E-02	2.24E-01	4.48E-04	3.43E-02

TABLE III. **Population 2** Processing Conditions

Sample	Paper Beam			PZR					Sensor Properties				Measurements		
ID	l	ω	t	l	CSA	t	Loc	C.P.	GF	ν	ρ	$\Delta R/R_0$	ε_x	ΔR_x	$\Delta R/\Delta X$
26	44.15	10	0.26	8	46.25	0.0126	0	SP	1.68E-02	5.00E-01	1.10E+02	4.45E-03	2.65E-01	5.31E-04	6.00E-03
27	39.15	10	0.26	8	46.25	0.0126	0	SP	4.47E-02	5.00E-01	1.10E+02	8.29E-03	1.86E-01	3.71E-04	1.02E-02
28	34.15	10	0.26	8	46.25	0.0126	0	SP	3.89E-02	5.00E-01	1.10E+02	7.03E-03	1.81E-01	3.61E-04	1.03E-02
29	29.15	10	0.26	8	46.25	0.0126	0	SP	5.02E-02	5.00E-01	1.10E+02	7.27E-03	1.45E-01	2.90E-04	1.15E-02
30	24.15	10	0.26	8	46.25	0.0126	0	SP	3.04E-02	5.00E-01	1.10E+02	5.83E-03	1.92E-01	3.84E-04	9.70E-03
31	19.15	10	0.26	8	46.25	0.0126	0	SP	1.88E-02	5.00E-01	1.10E+02	5.14E-03	2.73E-01	5.46E-04	8.80E-03
32	44.15	10	0.26	8	46.25	0.0126	0	SP	1.45E-02	5.00E-01	1.10E+02	3.29E-03	2.26E-01	4.53E-04	4.10E-03
33	44.15	10	0.52	8	46.25	0.0126	0	SP	9.15E-02	5.00E-01	1.10E+02	1.13E-02	1.24E-01	2.48E-04	8.30E-03
34	44.15	10	0.78	8	46.25	0.0126	0	SP	1.50E-01	5.00E-01	1.10E+02	1.22E-02	8.13E-02	1.63E-04	1.39E-02
35	44.15	10	1.04	8	46.25	0.0126	0	SP	2.10E-01	5.00E-01	1.10E+02	1.47E-02	6.99E-02	1.40E-04	1.93E-02
36	44.15	10	1.3	8	46.25	0.0126	0	SP	1.91E-01	5.00E-01	1.10E+02	1.38E-02	7.24E-02	1.45E-04	2.01E-02

[1] X. Liu, M. O'Brien, M. Mwangi Thuo, X. Li, and G. Whitesides, "Paper-based piezoresistive mems force sensors," Proceedings of the IEEE International Conference on Micro Electro Mechanical Systems (MEMS) , 133 – 136 (2011).

[2] A. Dhanaghopal, "Damping mechanisms in a tip=mass piezoelectric cantilever system," American Institute of Physics (AIP) **Submitted For Publication**.

[3] A. Martin, B. Chang, Z. Martin, D. Paramanik, C. Frankiewicz, S. Kundu, I. Tevis, and M. Mwangi Thuo, "Heat-free fabrication of metallic interconnects for flexible/wearable devices," Advanced Functional Materials **29**, 1903687 (2019).

[4] K. Senthil Kumar and P.-Y. Chen, "A review of printable flexible and stretchable tactile sensors," Research **2019** (2019), 10.34133/2019/3018568.

[5] D. Inman, "A distributed parameter electromechanical model for cantilevered piezoelectric energy harvesters," Journal of Vibration and Acoustics **130** (2008), 10.1115/1.2890402.

[6] A. Martin, C. Du, A. M. Pauls, T. Ward III, and M. Thuo, "Polydispersity-driven printing of conformal solid metal traces on non-adhering biological surfaces," Advanced Materials Interfaces **7**, 2001294 (2020), https://onlinelibrary.wiley.com/doi/pdf/10.1002/admi.202001294.

[7] A. Martin, B. S. Chang, A. M. Pauls, C. Du, and M. Thuo, "Stabilization of undercooled metals via passivating oxide layers," Angewandte Chemie International Edition **60**, 5928–5935 (2021), https://onlinelibrary.wiley.com/doi/pdf/10.1002/anie.202013489.

[8] B. S. Chang, R. Tutika, J. Cutinho, S. Oyola-Reynoso, J. Chen, M. D. Bartlett, and M. M. Thuo, "Mechanically triggered composite stiffness tuning through thermodynamic relaxation (st3r)," Mater. Horiz. **5**, 416–422 (2018).

[9] M. Baghbanzadeh, F. C. Simeone, C. M. Bowers, K.-C. Liao, M. Thuo, M. Baghbanzadeh, M. S. Miller, T. B. Carmichael, and G. M. Whitesides, "Odd–even effects in charge transport across n-alkanethiolate-based sams," Journal of the American Chemical Society **136**, 16919–16925 (2014), pMID: 25380500, https://doi.org/10.1021/ja509436k.

[10] A. Martin, C. Du, B. Chang, and M. Thuo, "Complexity and opportunities in liquid metal surface oxides," Chemistry of Materials **32**, 9045–9055 (2020), https://doi.org/10.1021/acs.chemmater.0c02047.

[11] B. Chang, A. Martin, P. Gregory, S. Kundu, C. Du, M. Orondo, and M. Mwangi Thuo, "Functional materials through surfaces and interfaces," MRS Advances **3**, 1–13 (2018).

[12] J. J. Chang, A. Martin, C. Du, A. M. Pauls, and M. Thuo,

TABLE IV. **Population 3** Random Processing Conditions

Sample	Paper Beam			PZR				C.P.	Sensor Properties				Measurements		
ID	l	ω	t	l	CSA	t	Loc		GF	v	ρ	$\Delta R/R_0$	ε_x	ΔR_x	$\Delta R/\Delta X$
37	44.215	9.5	0.26	8	46.25	0.0126	0	FM	3.08E-02	5.00E-01	1.10E+02	7.58E-03	2.46E-01	4.91E-04	1.80E-03
38	44.215	8	0.26	8	46.25	0.0126	0	SP	3.62E-02	5.00E-01	1.10E+02	6.72E-03	1.91E-01	3.82E-04	9.77E-03
39	44.215	8	0.26	13	71.25	0.0126	0	FM	6.78E-02	5.00E-01	1.70E+02	1.52E-02	2.24E-01	4.48E-04	1.19E-02
40	44.215	12.5	0.26	8	46.25	0.0126	0	FM	5.70E-02	5.00E-01	1.10E+02	9.58E-03	1.69E-01	3.13E-04	1.16E-02
41	44.215	10.5	0.78	8	46.25	0.0126	0	FM	1.47E-01	5.00E-01	1.10E+02	1.06E-02	7.19E-02	1.44E-04	2.26E-02
42	44.215	8	3.9	8	46.25	0.0126	0	SP	8.50E-01	5.00E-01	1.10E+02	6.13E-02	1.34E-01	2.56E-04	1.51E-01
43	44.215	8	0.26	8	46.25	0.0126	0	FM*	3.08E-02	5.00E-01	1.10E+02	7.58E-03	2.46E-01	4.91E-04	1.80E-03

"Heat-free biomimetic metal molding on soft substrates," Angewandte Chemie International Edition **59**, 16346–16351 (2020), https://onlinelibrary.wiley.com/doi/pdf/10.1002/anie.202008621.

[13] B. S. Chang, M. Fratzl, A. Boyer, A. Martin, H. C. Ahrenholtz, I. De Moraes, J.-F. Bloch, N. M. Dempsey, and M. M. Thuo, "Rapid prototyping of reconfigurable microfluidic channels in undercooled metal particle-elastomer composites," Industrial & Engineering Chemistry Research **58**, 4137–4142 (2019), https://doi.org/10.1021/acs.iecr.8b06441.

[14] L. Wei, X. Xu, G. Dayal, J. Bullock, and J. Ager, "Machine learning optimization of p-type transparent conducting films," Chem. Mater. **31** (2019), 10.1021/acs.chemmater.9b01953.

[15] B. Cao, L. A. Adutwum, A. O. Oliynyk, E. J. Luber, B. C. Olsen, A. Mar, and J. M. Buriak, "How to optimize materials and devices via design of experiments and machine learning: Demonstration using organic photovoltaics," ACS Nano **12**, 7434–7444 (2018), pMID: 30027732, https://doi.org/10.1021/acsnano.8b04726.